Sunyaev-Zel'dovich observation of the Bullet-like cluster Abell 2146 with the Arcminute Microkelvin Imager [*]

AMI Consortium: Carmen Rodríguez-Gonzálvez[1]† Malak Olamaie,[1]‡
Matthew L. Davies,[1] Andy C. Fabian,[2] Farhan Feroz,[1]
Thomas M. O. Franzen,[1] Keith J. B. Grainge,[1,3] Michael P. Hobson,[1]
Natasha Hurley-Walker,[1] Anthony N. Lasenby,[1,3] Guy G. Pooley,[1]
Helen R. Russell,[2] Jeremy S. Sanders,[2] Richard D. E. Saunders,[1,3]
Anna M. M. Scaife,[4] Michel P. Schammel,[1] Paul F. Scott,[1]
Timothy W. Shimwell,[1] David J. Titterington,[1] Elizabeth M. Waldram,[1]
and Jonathan T. L. Zwart[5]

[1] *Astrophysics Group, Cavendish Laboratory, 19 J. J. Thomson Avenue, Cambridge CB3 0HE*
[2] *Institute of Astronomy, Madingley Road, Cambridge CB3 0HA*
[3] *Kavli Institute for Cosmology Cambridge, Madingley Road, Cambridge, CB3 0HA*
[4] *Dublin Institute for Advanced Studies, 31 Fitzwilliam Place, Dublin 2, Ireland*
[5] *Columbia Astrophysics Laboratory, Columbia University, 550 West 120th Street, New York, NY 10027, USA*

ABSTRACT

We present $13.9-18.2$-GHz observations of the Sunyaev-Zel'dovich (SZ) effect towards Abell 2146 using the Arcminute Microkelvin Imager (AMI). The cluster is detected with a peak signal-to-noise ratio of 13σ in the radio source subtracted map from 9 hours of data. Comparison of the SZ image with the X-ray image from Russell et al. (2010) suggests that both have extended regions which lie approximately perpendicular to one another, with their emission peaks significantly displaced. These features indicate non-uniformities in the distributions of the gas temperature and pressure, and suggest complex dynamics indicative of a cluster merger. We use a fast, Bayesian cluster analysis to explore the high-dimensional parameter space of the cluster-plus-sources model to obtain robust cluster parameter estimates in the presence of radio point sources, receiver noise and primordial CMB anisotropy; despite the substantial radio emission from the direction of Abell 2146, the probability of SZ + CMB primordial structure + radio sources + receiver noise to CMB + radio sources + receiver noise is 3×10^6 : 1. We compare the results from three different cluster models. Our preferred model exploits the observation that the gas fractions do not appear to vary greatly between clusters. Given the relative masses of the two merging systems in Abell 2146, the mean gas temperature can be deduced from the virial theorem (assuming all of the kinetic energy is in the form of internal gas energy) without being affected significantly by the merger event, provided the primary cluster was virialized before the merger. In this model we fit a simple spherical isothermal β-model to our data, despite the inadequacy of this model for a merging system like Abell 2146, and assume the cluster follows the mass-temperature relation of a virialized, singular, isothermal sphere. We note that this model avoids inferring large-scale cluster parameters internal to r_{200} under the widely used assumption of hydrostatic equilibrium. We find that at r_{200} the average total mass $M_T = (4.1 \pm 0.5) \times 10^{14} h^{-1} M_\odot$ and the mean gas temperature $T = 4.5 \pm 0.5$ keV.

1 INTRODUCTION

Galaxy clusters are the largest collapsed structures known to exist in the Universe. The masses of rich clusters can reach $\approx 10^{15} h^{-1} M_\odot$ and the more distant ones, from around $z > 0.2$, subtend several arcminutes on the sky due to the slow variation of the angular diameter distance with redshift. As a result, clusters are powerful

tracers of structure formation and evolution on scales of the order of a few megaparsecs. According to the standard Λ Cold Dark Matter (ΛCDM) model, galaxy clusters form via hierarchical interactions of smaller subsystems. During merger, these subclusters collide at relative velocities of thousands of kms^{-1} and can release gravitational binding energies of up to $\sim 10^{57}$ J, which can lead

to shocks in the intracluster medium (IM). These conditions make cluster mergers ideal places to study the dynamics of matter under extreme conditions. The three assumed main components comprising the cluster, namely galaxies, hot ionized gas and dark matter, exhibit very different behaviours during subcluster mergers. The hot intergalactic gas is heated and compressed by the hydrodynamical shocks produced during the passage of the subcluster through the core of the primary, whereas the dark matter and galaxies are collisionless (see e.g. Markevitch et al. (2007)). As a result, the gas is slowed down by ram pressure and is displaced from the dark matter and the galaxies. Later, when the subcluster reaches regions of lower gas density in the primary cluster, the ram pressure drops sharply. Without as much ram pressure, the gas pressure and subcluster gravity cause some of the subcluster gas, which had been lagging behind the subcluster's dark matter centre, to 'slingshot' past it. This gas is then left unbound from the subcluster and free to expand adiabatically (Hallman et al. 2004).

Abell 2146 is a cluster at $z = 0.23$ consisting of two merging subclusters. The smaller subcluster passed through the centre of the larger subcluster some $0.1 - 0.3$ Gyrs ago producing shock fronts which have been detected by Chandra (Russell et al. 2010). These shock fronts are unusual features which only show at a specific stage in the cluster merger, before the shock reaches the outer, low-surface-brightness regions, and at angles on the sky plane which usually prevents the projection from hiding the density edge. Therefore, it is not surprising that shock fronts with Mach numbers significantly greater than one have only been detected in two other clusters: 1E0657-56 (Markevitch et al. 2002) –the "Bullet cluster"– and A520 (Markevitch 2006). Unlike A520, the Bullet cluster and Abell 2146 appear to be at an early stage of the merger event, where the cluster dynamics are simpler and the separation of the hot gas and the dark matter components is clearer.

The thermal Sunyaev-Zeldovich (SZ) effect provides an independent way of exploring the physics of the intracluster gas and examining typical cluster parameters such as core radius and gas mass. When Cosmic Microwave Background (CMB) photons traverse a rich galaxy cluster some will be inverse-Compton scattered by the random thermal motion of the electrons in the intracluster gas (Sunyaev & Zel'dovich 1970; Birkinshaw 1999). Unlike X-ray surface brightness, SZ surface brightness is independent of redshift and is therefore well suited for the study of galaxy clusters at any redshift. It is also less sensitive than X-ray measurements to small-scale clumping and the complex dynamics associated with the cluster core.

In this paper we present 16-GHz SZ effect images of Abell 2146 using AMI. In Section 2 we discuss the telescope, while details of the observations and the reduction pipeline are given in Section 3. In Section 4 Bayesian inference is introduced. Section 5 describes our analysis methodology while in Section 6 and Section 7 we present the results and discuss their significance. We present our conclusions in Section 8.

Throughout the paper we assume a concordance ΛCDM cosmology with $\Omega_{m,0} = 0.3$, $\Omega_{\Lambda,0} = 0.7$, $\Omega_k = 0$, $\Omega_b = 0.041$, $w_0 = -1$, $w_a = 0$, $\sigma_8 = 0.8$ and $H_0 = 100 \, \mathrm{km \, s^{-1} Mpc^{-1}}$. Relevant parameters are given in terms of the dimensionless Hubble parameter $h = H_0/100 \, \mathrm{km \, s^{-1} \, Mpc^{-1}}$, except where otherwise stated. We also refer to $h_X = H_0/X \, \mathrm{km \, s^{-1} \, Mpc^{-1}}$. All coordinates are at epoch J2000.

Table 1. AMI technical summary

	SA	LA
Antenna diameter	3.7 m	12.8 m
Number of antennas	10	8
Baseline lengths (current)	$5 - 20$ m	$18 - 110$ m
Primary beam at 15.7 GHz	$20'.1$	$5'.5$
Synthesized beam	$\approx 3'$	$\approx 30''$
Flux sensitivity	30 mJy s$^{-1/2}$	3 mJy s$^{-1/2}$
Observing frequency	$13.9 - 18.2$GHz	$13.9 - 18.2$GHz
Bandwidth	4.3 GHz	4.3 GHz
Number of channels	6	6
Channel bandwidth	0.72 GHz	0.72 GHz

Table 2. Assumed I+Q flux densities of 3C286 and 3C48, and errors on flux measurements in each frequency channel, over the commonly-used AMI SA bandwidth.

Channel	ν/GHz	S^{3C286}/Jy	S^{3C48}/Jy	σ_S
3	14.2	3.61	1.73	6.5%
4	15.0	3.49	1.65	5.0%
5	15.7	3.37	1.57	4.0%
6	16.4	3.26	1.49	3.5%
7	17.1	3.16	1.43	4.0%
8	17.9	3.06	1.37	7.0%

2 THE TELESCOPE

AMI comprises two arrays: the Small Array (SA) which consists of ten 3.7-m diameter antennas, and the Large Array (LA) with eight 13-m antennas, located at Lord's Bridge, Cambridge (AMI Consortium: Zwart et al. 2008). The higher resolution and flux sensitivity of the LA allows contaminating radio sources to be dealt with. These sources can then be subtracted from the SA maps. A summary of the technical details of AMI is given in Table 1. Further details on the telescope can be found in AMI Consortium: Zwart et al. (2008).

3 OBSERVATIONS AND DATA REDUCTION

Observations of Abell 2146 were made by the SA and LA between November 2009 and March 2010, yielding approximately 9 hours of good quality SA data; approximately the same amount of data suffered from artifacts and was discarded. Data reduction was perfomed using REDUCE, a local software tool developed for the Very Small Array (VSA) (Watson et al. 2003) and AMI (see e.g. AMI Consortium: Zwart et al. (2008) for further details). This package is designed to apply path delay corrections and a series of algorithms tailored to remove automatically bad data points arising from interference, shadowing, hardware and other errors. We apply amplitude clips at a 3σ level. Periods where the data has been

contaminated by interference are excised. These interference signals are identified as persistent high amplitude signals in the lag domain, which appear in all the lag channels. The system temperature is monitored by a modulated noise signal sent to the front-end of each antenna and synchronously detected at the end of each intermediate-frequency channel and is used in REDUCE to correct the amplitude scale on an antenna basis. If the system temperature falls below 10% of the nominal value of an antenna the associated datapoints are removed. For further details on the AMI reduction pipeline see Hurley-Walker (2009). Additional manual flagging of remaining bad data points is done to ensure the quality of the data. The correlator data are then Fourier transformed into the frequency domain and stored on disk in FITS format.

Flux calibration was performed using short observations of primary calibrators, either 3C48 or 3C286. The flux densities for 3C48 and 3C286, see Table 2, are in agreement with Baars et al. (1977) at 16-GHz. Since Baars et al. (1977) measure I, as opposed to AMI which measures I + Q, the flux densities were corrected by interpolating from VLA 5-, 8- and 22- GHz observations. Previous tests have shown this calibration to be accurate to better than 5 per cent (AMI Consortium: Scaife et al. 2009). The phase is calibrated using interleaved calibrators selected from the Jodrell Bank VLA Survey (Patnaik et al. 1992; Browne et al. 1998; Wilkinson et al. 1998) based on their proximity and flux density. The phase calibrators used for the observations of Abell 2146 were J1642+6856 for the SA and J1623+6624 for the LA. These phase calibrators were interleaved approximately every hour for the SA and every ten minutes for the LA.

3.1 Source subtraction

Contamination from radio point sources at $\approx$ 15 GHz can significantly obscure the SZ signal and must therefore be taken into account in any SZ effect analyses at these frequencies. The higher resolution and flux sensitivity of the LA is exploited to determine the position of the sources in the SA maps accurately in a short amount of time. Local maxima on the continuum LA maps above $4\sigma_n$, where σ_n is the corresponding value in Janskys per beam at that pixel in the noise map, are identified as LA detected sources using AMI-developed source extraction software (see AMI Consortium: Franzen et al. (2010)). Out of these LA-detected sources only those which appear within 0.1 of the SA power primary beam having an apparent flux above $4\sigma_n$ on the SA map are included in the source model.

Every source in the source model is parameterized by a position, a spectral index and a flux density whose priors are based on the LA measurements. The source model is analysed by McADAM (Monte Carlo Astronomical Detection and Measurement), a Bayesian analysis package for cluster detection and parameter extraction developed by Marshall et al. (2003) and adapted for AMI by Feroz et al. (2009), which fits a probability distribution to the source flux densities at the positions given by the LA. The source flux densities are fitted by McADAM to allow for possible intercalibration difference between the two AMI arrays and for source variability. The mean source flux-density values are then used to subtract the sources from the SA map.

4 BAYESIAN ANALYSIS OF CLUSTERS

4.1 Bayesian inference

The cluster analysis software implemented in this paper (Marshall et al. 2003) is based on Bayesian inference. This robust methodology constrains a set of parameters, $\boldsymbol{\Theta}$, given a model or hypothesis, H and the corresponding data, $\boldsymbol{D}$, using Bayes' theorem:

$$\Pr(\boldsymbol{\Theta}|\boldsymbol{D}, H) \equiv \frac{\Pr(\boldsymbol{D}|\boldsymbol{\Theta}, H)\,\Pr(\boldsymbol{\Theta}|H)}{\Pr(\boldsymbol{D}|H)}. \qquad (1)$$

Here $\Pr(\boldsymbol{\Theta}|\boldsymbol{D}, H) \equiv P(\boldsymbol{\Theta})$ is the posterior probability distribution of the parameters, $\Pr(\boldsymbol{D}|\boldsymbol{\Theta}, H) \equiv \mathcal{L}(\boldsymbol{\Theta})$ is the likelihood, $\Pr(\boldsymbol{\Theta}|H) \equiv \pi(\boldsymbol{\Theta})$ is the prior probability distribution and $\Pr(\boldsymbol{D}|H) \equiv \mathcal{Z}$ the Bayesian evidence. If chosen wisely, incorporating the prior knowledge into the analysis reduces the amount of parameter space to be sampled and allows meaningful model selection. Bayesian inference can serve as a tool for two main purposes:

(i) Parameter estimation—In this case, the evidence factor can be neglected since it is independent of the model parameters, $\boldsymbol{\Theta}$. Sampling techniques can then be used to explore the unnormalized posterior distributions. One obtains a set of samples from the parameter space distributed according to the posterior. Constraints on individual parameters can then be obtained by marginalising over the other parameters.

(ii) Model selection—The evidence is crucial for ranking models for the data. It is defined as the factor required for normalising the posterior over $\boldsymbol{\Theta}$:

$$\mathcal{Z} = \int \mathcal{L}(\boldsymbol{\Theta})\pi(\boldsymbol{\Theta})d^D\boldsymbol{\Theta}, \qquad (2)$$

where D is the dimensionality of the parameter space. This factor represents an average of the likelihood over the prior and will therefore favour models with high likelihood values throughout the entirety of parameter space. This satisfies Occam's razor which states that the evidence will be larger for simple models with compact parameter spaces than for more complex ones, unless the latter fit the data significantly better. Deciding which of two models, H_0 and H_1, best fits the data can be done by computing the ratio

$$\frac{\Pr(H_1|\boldsymbol{D})}{\Pr(H_0|\boldsymbol{D})} = \frac{\Pr(\boldsymbol{D}|H_1)\Pr(H_1)}{\Pr(\boldsymbol{D}|H_0)\Pr(H_0)} = \frac{\mathcal{Z}_1}{\mathcal{Z}_0}\frac{\Pr(H_1)}{\Pr(H_0)}, \qquad (3)$$

where $\frac{\Pr(H_1)}{\Pr(H_0)}$ is the prior probability ratio set before any conclusions have been drawn from the dataset.

4.2 Nested sampling

Nested sampling is a Monte Carlo method introduced by Skilling et al. (2004) which focuses on the efficient calculation of evidences and generates posterior distributions as a by-product. Feroz & Hobson (2008) and Feroz, Hobson & Bridges (2009) have developed this sampling framework and implemented the MULTI-NEST algorithm. This algorithm can sample from posterior distributions where multiple modes and/or large (curving) degeneracies are present. This robust technique has reduced by a factor of $\approx$ 100 the computational costs incurred during Bayesian parameter estimation and model selection. For this reason the analysis in this paper is based on this technique.

5   PHYSICAL MODEL AND ASSUMPTIONS

5.1   Interferometric data model

An interferometer, like AMI, operating at a frequency, ν, measure samples from the complex visibility plane $\widetilde{I_\nu}(\boldsymbol{u})$. These are given by a weighted Fourier transform of the surface brightness, $I_\nu(\boldsymbol{x})$:

$$\widetilde{I_\nu}(\boldsymbol{u}) = \int A_\nu(\boldsymbol{x})I_\nu(\boldsymbol{x})\exp(2\pi i \boldsymbol{u} \cdot \boldsymbol{x})\mathrm{d}^2\boldsymbol{x}, \tag{4}$$

where $\boldsymbol{x}$ is the position relative to the phase centre, $A_\nu(\boldsymbol{x})$ is the (power) primary beam of the antennas at an observing frequency, ν (normalized to unity at its peak) and $\boldsymbol{u}$ is the baseline vector in units of wavelength. In our model we assume the measured visibilities can be defined as

$$V_\nu(\boldsymbol{u}_i) = \widetilde{I_\nu}(\boldsymbol{u}_i) + N_\nu(\boldsymbol{u}_i), \tag{5}$$

where $\widetilde{I_\nu}(\boldsymbol{u})$ is the signal component, which contains contributions from the cluster SZ effect signal and identified radio point sources and $N_\nu(\boldsymbol{u}_i)$ is a generalized noise component that includes signals from unresolved point sources, primordial CMB anisotropies and instrumental noise.

5.2   Cluster models

In order to calculate the contribution of the cluster SZ signal to the visibility data the Comptonization parameter of the cluster, $y(s)$, across the sky must be determined (see Feroz et al. (2009) for further details). This parameter is the integral of the gas pressure along the line of sight l through the cluster:

$$y(s) = \frac{\sigma_T}{m_e c^2} \int_{-\infty}^{\infty} n_e k_B T \mathrm{d}l \propto \int_{-r_{\mathrm{lim}}}^{+r_{\mathrm{lim}}} \rho_g T \mathrm{d}l, \tag{6}$$

where σ_T is the Thomson scattering cross-section, n_e is the electron number density, which is derived from equation (9), m_e is the electron mass, c is the speed of light and k_B is the Boltzmann constant. $s = \theta D_\theta$ is the deprojected radius such that $r^2 = s^2 + l^2$ and D_θ is the angular diameter distance to the cluster which can be calculated for clusters at redshifts, z, using

$$D_\theta = \frac{c \int_0^z H^{-1}(z')\,\mathrm{d}z'}{(1+z)}. \tag{7}$$

We set r_{lim} in equation (6) to $20h^{-1}\mathrm{Mpc}$—this result has been tested and shown to be large enough even for small values of β (Marshall et al. 2003).

The cluster geometry, as well as two linearly independent functions of its temperature and density profiles, must be specified to compute the Comptonization parameter. For the cluster geometry we have chosen a spherical cluster model as a first approximation. The temperature profile is assumed to be constant throughout the cluster. An isothermal β-model is assumed for the cluster gas density, ρ_g (Cavaliere & Fusco-Fermiano 1978):

$$\rho_g(r) = \frac{\rho_g(0)}{\left[1 + \left(\frac{r}{r_c}\right)^2\right]^{\frac{3\beta}{2}}}, \tag{8}$$

where

$$\rho_g(r) = \mu_e n_e(r), \tag{9}$$

$\mu_e = 1.14m_p$ is the gas mass per electron and m_p is the proton mass. The core radius, r_c, gives the density profile a flat top at low $\frac{r}{r_c}$ and ρ_g has a logarithmic slope of 3β at large $\frac{r}{r_c}$.

Parameter estimates can depend on the way the cluster model is parameterized. We examine the impact of different physical assumptions by presenting the parameter estimates for Abell 2146 obtained using three different cluster parameterizations (or 'models'). Modelled sources for all three models are characterised by three parameters: position, flux density and spectral index. The corresponding priors for these parameters are given in Section 5.3.2. The parameterizations of the sources and the source priors are the same in all three models, unlike the cluster parameterizations which do change between models. The mean values fitted by our McAdam software to both the source and cluster sampling parameters will, however, vary for each cluster model. We proceed to describe our three cluster parameterizations and their results.

Tables 4 and 3 indicate which parameters are derived in each model and the assumptions made in each case. A summary of the sampling parameters for each model together with their priors is given in Table 5.

5.2.1   Cluster model 1

Our first model, henceforth M1, is based on traditional methods for the analysis of SZ and X-ray data. The sampling parameters for M1 are:

- (x_c, y_c)—the position of the cluster centroid on the sky.
- T—the temperature of the cluster gas, which is assumed to be uniform.
- β—defines the outer logarithmic slope of the β-profile.
- r_c—gives the density profile a flat top at low r
- $M_g(r_{200})$—the gas mass inside a radius, r_{200}, which is the radius at which the average total density is 200 times ρ_{crit}, the critical density for closure of the Universe.
- z—the cluster redshift.

In applying this cluster model to Abell 2146 both z and T are assumed to be known, which is equivalent to assigning them delta-function priors (see Table 5) .

The derived parameters for M1 are:

- r_X—the radius at which the average total density is X times ρ_{crit}.
- $M_T(r_X)$—the total cluster mass within the radius r_X.
- $M_g(r_X)$—the cluster gas mass within the radius r_X.
- $f_g(r_X)$—the cluster average gas fraction within the radius r_X.
- $\rho_g(0)$—the central gas density.
- $y(0)$—the central Comptonization parameter.

In this model, the cluster gas is assumed to be in hydrostatic equilibrium with the total gravitational potential of the cluster, Φ, which is dominated by dark matter. As a result, the gravitational potential must satisfy

$$\frac{\mathrm{d}\Phi}{\mathrm{d}r} = -\frac{1}{\rho_g}\frac{\mathrm{d}p}{\mathrm{d}r}. \tag{10}$$

This equation can be simplified if the cluster gas consists purely of ideal gas with a uniform temperature, T, to give

$$\frac{\mathrm{d}\log\rho_g}{\mathrm{d}\log r} = -\frac{G\mu}{k_B T}\frac{M_T(r)}{r}, \tag{11}$$

where μ is the mass per particle, $\mu \approx 0.6m_p \approx \frac{0.6}{1.14}\mu_e$ (see Marshall et al. 2003). Expressions for the total mass of the cluster, $M_T(r_X)$, can be obtained for spherical symmetry:

$$M_T(r_X) = \frac{4\pi}{3}r_X^3 X\rho_{crit}, \tag{12}$$

or by integrating the isothermal β-model for the density profile in (11),

$$M_{\mathrm{T}}(r_X) = \frac{r_X^3}{r_\mathrm{c}^2 + r_X^2} \frac{3\beta \mathrm{k_B} T}{\mathrm{G}\mu}. \qquad (13)$$

Combining equations (12) and (13) leads to an expression for r_X,

$$r_X = \sqrt{\frac{9\beta \mathrm{k_B} T}{4\pi \mu \mathrm{GX}\rho_{\mathrm{crit}}} - r_\mathrm{c}^2}. \qquad (14)$$

The total mass of the cluster within a certain radius, $M_{\mathrm{T}}(r_X)$, is subsequently determined by substituting r_X into equation (12). Once $M_{\mathrm{T}}(r_X)$ and $M_{\mathrm{g}}(r_X)$ are known, the gas fraction, $f_{\mathrm{g}}(r_X)$, can be computed using the relation

$$f_{\mathrm{g}}(r_X) = \frac{M_{\mathrm{g}}(r_X)}{M_{\mathrm{T}}(r_X)}. \qquad (15)$$

We consider values for $X = 200$ and 500. For $X = 500$, $M_{\mathrm{g}}(r_X)$ is not a sampling parameter but is calculated using the expression

$$M_{\mathrm{g}}(r_X) = \rho_{\mathrm{g}}(0) \int_0^{r_X} \frac{4\pi r'^2}{\left[1 + \frac{r'^2}{r_\mathrm{c}^2}\right]^{\frac{3\beta}{2}}} \mathrm{d}r', \qquad (16)$$

Also, $\rho_{\mathrm{g}}(0)$, in equation (8), can be recovered by numerically integrating the gas density profile up to r_{200}, equation (16), and setting the result equal to $M_{\mathrm{g}}(r_{200})$.

5.2.2 Cluster model 2

Our second model, M2, has the same sampling parameters as M1 with the exception of T, which becomes a derived parameter, and $f_{\mathrm{g}}(r_{200})$, which becomes a sampling parameter. Sampling from $f_{\mathrm{g}}(r_{200})$ and $M_{\mathrm{g}}(r_{200})$ allows $M_{\mathrm{T}}(r_{200})$ to be calculated using equation (15). r_{200} can then be computed simply by rearranging equation (12). The temperature of the cluster gas can be obtained by combining equations (11) and (8) to yield

$$T = \frac{\mathrm{G}\mu}{3\mathrm{k_B}\beta} \frac{M_{\mathrm{T}}(r_{200})(r_\mathrm{c}^2 + r_{200}^2)}{r_{200}^3}, \qquad (17)$$

which is based upon the assumption that the cluster is in hydrostatic equilibrium and described well by a β-profile. The derived parameters at r_{500} are calculated in the same way as in M1; once $M_{\mathrm{g}}(r_{500})$ is obtained from equation (16) and r_{500} from equation (14), $M_{\mathrm{T}}(r_{500})$ is calculated by assuming the cluster is spherical, equation (12). $f_{\mathrm{g}}(r_{500})$ can then be recovered using the relation in (15) .

5.2.3 Cluster model 3

In the third model, M3, the sampling and derived parameters are the same as in M2. The only difference between M2 and M3 is the way T is calculated. M3 uses an M-T relation to derive T which allows T to be obtained without relying on the cluster being in hydrostatic equilibrium, a necessary assumption in M2. Moreover, at r_{200}, all the other cluster parameter estimates of M3 are free from the assumption of hydrostatic equilibrium. However, this assumption needs to be made to obtain cluster parameters at r_{500} (see Section 5.2.2).

If the cluster is assumed to be virialized and to contain a small amount of unseen energy density in the form of turbulence, bulk motions or magnetic fields, the average cluster gas temperature, T, can be obtained using the mass-temperature (M-T) relation for a singular, isothermal sphere (SIS) based on the virial theorem,

$$\mathrm{k_B} T = \frac{\mathrm{G}\mu M_{\mathrm{T}}}{2r_{200}} \qquad (18)$$

$$= \frac{\mathrm{G}\mu}{2\left(\frac{3}{4\pi(200\rho_{\mathrm{crit}})}\right)^{1/3}} M_{\mathrm{T}}^{2/3} \qquad (19)$$

$$= 8.2\mathrm{keV}\left(\frac{M_{\mathrm{T}}}{10^{15}h^{-1}\mathrm{M_\odot}}\right)^{2/3}\left(\frac{H(z)}{H_0}\right)^{2/3}, \qquad (20)$$

where H is the Hubble parameter. In our cluster model we use the well-behaved β-profile, equation (8), rather than the SIS density profile which is singular at $r = 0$. This different choice for the density profile will introduce a factor to the M-T relation in equation (20). From cluster simulations we find that this factor varies between $0.7 - 1.2$.

5.2.4 M-T relation and hydrostatic equilibrium

The results obtained from running MᴄAᴅᴀᴍ with three different models are useful for assessing the validity of some of the assumptions made in each model. Traditional models tend to assume clusters are isothermal, spherical, virialized and in hydrostatic equilibrium. All of these assumptions are particularly inappropriate for cluster mergers like Abell 2146. The first two assumptions are made in the three models presented in this paper to simplify the cluster model; but note that the spherical assumption is not bad here because our SZ measurements are sensitive to the larger scales of the cluster.

M2 also assumes hydrostatic equilibrium to obtain an estimate for T. After the gravitational collapse of a cluster, the hot gas in the ICM tends to reach equilibrium when the force exerted by the thermal pressure gradient of the ICM balances that from the cluster's own gravitational force. An underlying assumption is that the gas pressure is provided entirely by thermal pressure. In reality, there are many non-thermal sources of pressure support present in most clusters such as turbulent gas motions which can provide $\approx 10 - 20\%$ of the total pressure support even in relaxed clusters (Schuecker, Bohringer and Voges 2004; Rasia et al. 2006). In the case of Abell 2146, a complex merging system with two detected shocks propagating at ≈ 1900 and $2200\mathrm{kms}^{-1}$ (Russell et al. 2010), there is significant non-thermal pressure support provided by bulk motions in the ICM.

Relating radius, temperature and total mass via the virial theorem in practice also assumes that the kinetic energy is in the form of internal energy of the particles, as evidenced by the SZ signal, so that turbulent motions, bulk motions and everything else are ignored. But this use of the virial theorem has an advantage over hydrostatic equilibirum in the case of Abell 2146 since our knowledge of the mass ratio of the two merging systems enables us to set a limit on the degree to which the use of the M-T relation, $T \propto M_{\mathrm{T}}^{\frac{2}{3}}$, biases our temperature estimate.

Russell et al. (2010) find the fractional mass of the merging cluster to be between 25 and 33 percent, in which case the average temperature of the merging system will be $\approx 10\%$ higher when all the gas mass of the subcluster has merged with that of the primary cluster than prior to the start of the merger event. Therefore, provided the primary cluster was virialized pre-merger, our estimate for T using the M-T relation in equation (20) is little affected by the merger.

Table 4. Summary of the main assumptions made in the calculation of the derived parameters for each model. H stands for hydrostatic equilibrium, M-T for the mass-temperature relation given in equation (20) , B for isothermal β-profile, S for spherical geometry and N/A means not applicable, since that parameter is a sampling parameter for that particular model.

	Model Assumptions		
Derived Parameter	Model 1	Model 2	Model 3
r_{200}/h^{-1} Mpc	H, S, B; Eq. 14	S; Eq.12	S; Eq.12
$M_{\mathrm{T}}(r_{200})$	S; Eq.12	Eq.15	Eq.15
$f_{\mathrm{g}}(r_{200})/h^{-1}$	Eq.15	N/A	N/A
$M_{\mathrm{g}}(r_{500})/h^{-2}\mathrm{M}_\odot$	S, B; Eq.16	S, B; Eq.16	S, B; Eq.16
r_{500}/h^{-1} Mpc	H, S, B; Eq.14	H, S, B; Eq.14	H, S, B; Eq.14
$M_{\mathrm{T}}(r_{500})$	S; Eq.12	S; Eq.12	S; Eq.12
$f_{\mathrm{g}}(r_{500})/h^{-1}$	Eq.15	Eq.15	Eq.15
T keV	N/A	H; Eq.17	M-T; Eq.20

Table 3. Summary of the derived parameters for each cluster model.

Derived Parameter	Model
r_{200} & r_{500}/h^{-1} Mpc	All
$M_{\mathrm{T}}(r_{200})$ & $M_{\mathrm{T}}(r_{500})/h^{-1}\mathrm{M}_\odot$	All
$M_{\mathrm{g}}(r_{500})/h^{-2}\mathrm{M}_\odot$	All
y	All
n_{e}	All
T keV	M2, M3
$f_{\mathrm{g}}(r_{200})/h^{-1}$	M1
$f_{\mathrm{g}}(r_{500})/h^{-1}$	All

5.3   Priors

5.3.1   Cluster priors

For simplicity the priors are assumed to be separable. The priors used in the analysis of Abell 2146 are given in Table 5.

We note that, although the prior on $M_{\mathrm{g}}(r_{200})$ assumes the cluster produces a non-zero SZ effect, it is wide enough that our results will not be biased. In fact, our posterior distributions for $M_{\mathrm{g}}(r_{500})$ peak at $M_{\mathrm{g}}(r_{500}) > 3 \times 10^{13}/h^{-2}\mathrm{M}_\odot$ and have fallen to zero by $M_{\mathrm{g}}(r_{500}) > 2 \times 10^{13}/h^{-2}\mathrm{M}_\odot$, while our prior for $M_{\mathrm{g}}(r_{200})$ extends down to $1 \times 10^{13}/h^{-2}\mathrm{M}_\odot$

The prior on the gas mass fraction was set to a Gaussian centered at the WMAP7 best-fit value, $f_{\mathrm{g}} = 0.12h^{-1}$, with $\sigma = 0.016h^{-1}$. This result was obtained from WMAP7 estimates of $\Omega_{\mathrm{m}} = 0.266 \pm 0.029$, $\Omega_{\mathrm{b}} = 0.0449 \pm 0.0028$ and $h = 0.710 \pm 0.025$ using the relation $f_{\mathrm{b}} = \frac{\Omega_{\mathrm{b}}}{\Omega_{\mathrm{m}}}$, where f_{b} is the universal baryon fraction (Larson et al. 2010). The prior on f_{g} can be based on f_{b} since f_{g} in clusters at large radii approaches f_{b}. The prior on the position of the cluster was a Gaussian with $\sigma = 60''$ centered at the X-ray centroid.

5.3.2   Source priors

As with the cluster priors, the source priors are assumed to be separable, such that

$$\pi(\boldsymbol{\Theta}_S) = \pi(x_{\mathrm{s}})\,\pi(y_{\mathrm{s}})\,\pi(S_0)\,\pi(\alpha).$$

$\pi(x_{\mathrm{s}})$ and $\pi(y_{\mathrm{s}})$ are given delta priors at the source position found from the high-resolution LA maps. The flux-density priors for modelled sources on the other hand are chosen to be Gaussians centered on the flux-density value given by the LA with $\sigma \approx 40\%$ of the LA source flux. Tight constraints on the flux-density priors are best avoided due to inter-array calibration differences and source variability. The channel flux densities taken from the LA data are used to calculate an estimate for the spectral index of each source. The spectral index prior is then set as a Gaussian centered at the predicted LA value with a width $\sigma = 1$.

6   RESULTS

6.1   Maps and evidences

Fifteen sources were detected above $4\sigma_n$ on the LA map, Fig. 1. McAdam was used to determine the flux densities and spectral indices of these sources in the SA data. The standard AIPS tasks were used to clean the images with a single clean box. No primary beam correction has been applied to the AMI maps presented in this paper such that the thermal noise, σ_n, is constant throughout the map. The task imean was applied to the data to determine the noise level on the maps. Contours increasing linearly in units of σ_n were used to produce all the contour maps. The half-power contour of the synthesized beam for each map is shown at the bottom left of each map.

Further analysis was undertaken in the visibility plane taking into account receiver noise, radio sources, and contributions from primary CMB imprints. Figs 2 and 3 show the SA maps of Abell 2146 before and after radio source subtraction. The source subtraction was performed at the LA source position using the mean flux-density estimates given by the McAdam results of M3, Table 6. Sources with a high signal-to-noise ratio and close to the pointing centre tend to have good agreement between flux densities measured by the LA and those obtained by McAdam. Possible reasons

Table 5. Summary of the priors for the sampling parameters in each model.

Parameter	Models	Prior Type	Values	Origin
$x_c, y_c\,''$	all	gaussian at $\boldsymbol{x}_{\mathrm{X-ray}}, \sigma = 60''$	$15^h56^m07^s, +66°21'35''$	Ebeling et al. (2000)
β	all	uniform	$0.3 - 2.5$	Marshall et al. (2003)
$M_g(r_{200})/h^{-2}\mathrm{M}_\odot$	all	uniform in log	$10^{13} - 10^{15}$	physically reasonable
$r_c/h^{-1}\mathrm{kpc}$	all	uniform	$10 - 1000$	physically reasonable
z	all	delta	0.23	Ebeling et al. (2000)
$f_g(r_{200})/h^{-1}$	M2, M3	gaussian, $\sigma = 0.016$	0.12	Larson et al. (2010)
T keV	M1	delta	6.7	Russell et al. (2010)

for source flux-density discrepancies between the arrays, in particular for the remaining sources, include: a poorer fit of the Gaussian modelled primary beam at large *uv*-distances from the pointing centre, loss of signal due to the white light fringes falling off the end of the correlator, time and bandwidth smearing, correlator artifacts, source variability and, some sources with low signal-to-noise ratios detected on the LA, might appear as noise features on the SA.

It should be noted that, since a single flux-density value is used for subtracting the modelled sources in the map-plane, the radio source subtracted map does not reflect the uncertainty in the MCADAM derived flux-density estimates [1]. Nevertheless, flux-density estimates given by MCADAM have been tested in Feroz et al. (2009) and shown to be reliable. Fig. 9 shows that there is no degeneracy between the flux density fitted for source A in Fig. 3 and the fitted values for $M_g(r_{200})$, the cluster gas mass within r_{200} The detection of Abell 2146 in the AMI data is confirmed by comparing the evidence obtained by running MCADAM with a model including SZ + CMB primordial structure + radio sources + receiver noise and the null evidence, which corresponds to a model without a cluster, i.e. simply CMB + radio sources + receiver noise. The first model, which included an SZ feature, was found to be e^{15} times more probable than one without.
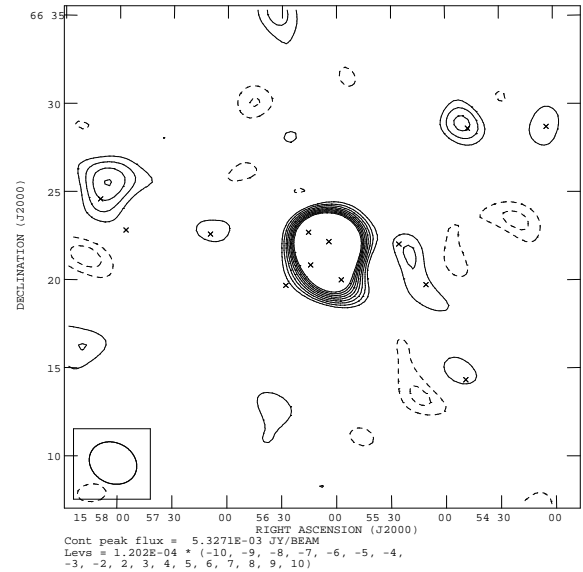
In Fig. 4 a 0.6-kλ taper is used to enhance large scale structure and consequently the signal-to-noise ratio of the SZ effect. The peak decrement in it is $\approx 13\sigma$.

The AMI SZ maps are compared to the Chandra X-ray emission and projected temperature maps for Abell 2146 in the discussion, Section 7.

### 6.2 Parameter estimates from three cluster models

MCADAM was run on the same Abell 2146 data for each of the three models described in 5.2. The results obtained for these models are shown in Figs 5 to 11. The contours in all the 2D marginalized posterior distributions represent 68% and 95% confidence limits. Axis labels for $M_g(r_{200})$ are in units of 10^{13} for clarity.

[1] Note that, unlike for the radio source subtracted maps, when obtaining estimates for the cluster parameters the whole probability distribution for the source flux density is taken into account, such that a larger uncertainty in the source flux densities will lead to wider distributions in the cluster parameters.


Cont peak flux = 5.8479E-03 JY/BEAM
Levs = 1.806E-04 * (-10, -9, -8, -7, -6, -5, -4, -3, 3, 4, 5, 6, 7, 8, 9, 10)

Figure 1. LA contour map.

Cont peak flux = 5.3271E-03 JY/BEAM
Levs = 1.202E-04 * (-10, -9, -8, -7, -6, -5, -4, -3, -2, 2, 3, 4, 5, 6, 7, 8, 9, 10)
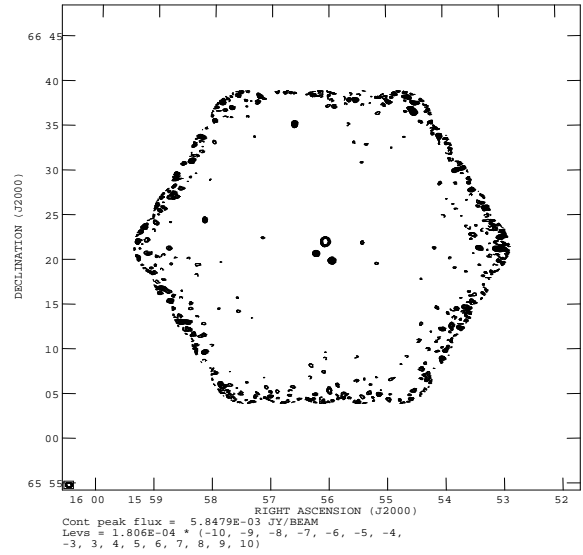
Figure 2. SA map before source subtraction. The crosses indicate the position of the sources detected on the LA map.

Table 6. List of the detected sources with their J2000 position coordinates, as determined by the LA map. Columns 3 and 4 show the flux densities of the detected sources at 16-GHz (S_{16}) given by McADAM using M3 with their associated Gaussian errors. For comparison, the LA measured flux densities at the same frequency are given. The letters represent the labeled sources in Fig. 3.

Source	RA (h m s)	Dec (° ′ ″)	McADAM-fitted S_{16}(mJy)	σ	LA S_{16}(mJy)
A	15 56 04.23	+66 22 12.94	5.92	0.18	5.95
B	15 54 30.95	+66 36 39.58	0.60	0.29	0.61
C	15 56 14.30	+66 20 53.45	1.83	0.14	1.70
D	15 56 36.51	+66 35 21.65	2.15	0.15	1.65
E	15 55 57.42	+66 20 03.11	1.65	0.08	1.64
F	15 58 10.23	+66 24 35.72	1.49	0.12	1.29
G	15 54 03.96	+66 28 41.90	1.12	0.15	0.74
H	15 55 25.67	+66 22 03.96	0.48	0.05	0.67
I	15 55 10.84	+66 19 45.82	0.61	0.06	0.65
J	15 57 09.46	+66 22 37.62	0.43	0.06	0.63
K	15 54 47.50	+66 28 37.43	0.91	0.09	0.53
L	15 54 49.11	+66 14 21.49	0.72	0.09	0.47
M	15 56 15.40	+66 22 44.48	0.16	0.07	0.43
N	15 56 27.90	+66 19 43.82	0.11	0.05	0.33
O	15 57 56.10	+66 22 49.80	0.30	0.07	0.49
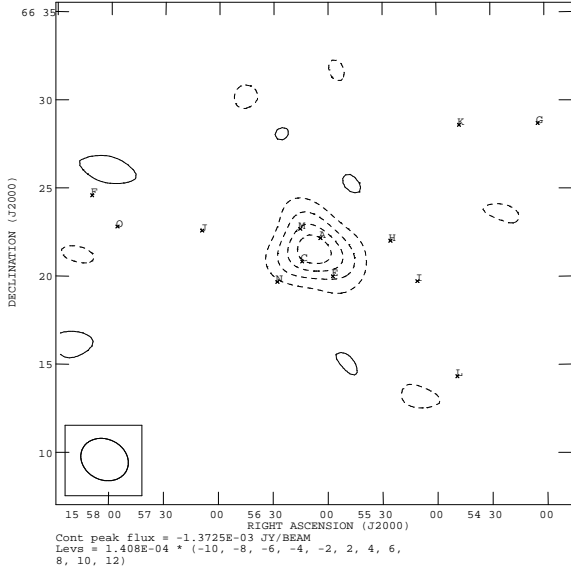
Figure 3. SA contour map after source subtraction. The letters represent the position of the sources detected on the LA map.
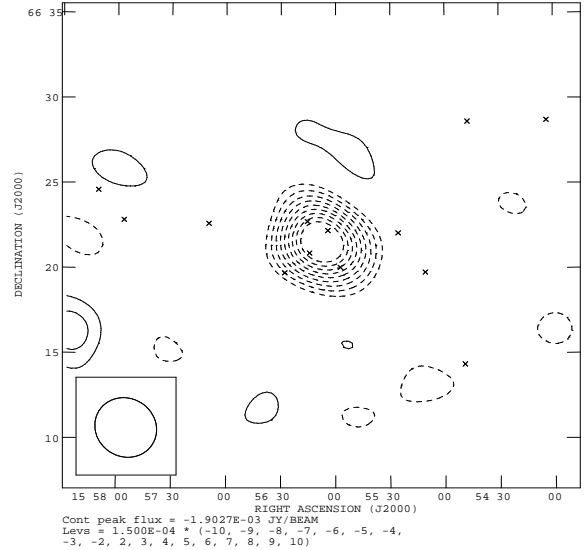
Figure 4. SA map after source subtraction using a 0.6-kλ taper. The crosses represent the position of the sources detected on the LA map.

6.2.1 Cluster model 1

The 2-D and 1-D marginalized posterior probability distributions for the parameters of M1 are depicted in Figs. 5 and 6, respectively.

M1 is representative of the more conventional method for extracting cluster parameters from SZ data. In this model, the average cluster gas temperature within r_{200} is assumed to be known, from X-ray measurements, allowing the morphology of the cluster, namely r_X, to be inferred by assuming the cluster is spherical, in hy-

drostatic equilibrium and described well by an isothermal β-model. The overall bias on r_X arises from all of these assumptions, which are particularly unphysical in a cluster merger like Abell 2146, and is therefore expected to be large. Indeed, by comparing Figs. 6 and 11 we find that r_{200} is overestimated with respect to the value obtained in M3, our most physically motivated model. Moreover, in M1, $M_g(r_X)$ for $X = 500$ and 1000 depends on r_X, which results in
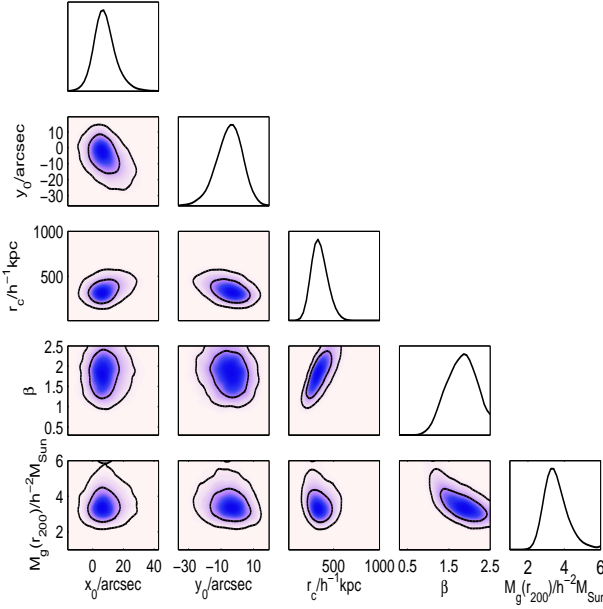
Figure 5. Two-dimensional marginalized posterior distributions for the sampling parameters of Abell 2146—M1.

Figure 7. Two-dimensional marginalized posterior distributions for the sampling parameters of Abell 2146—M2.
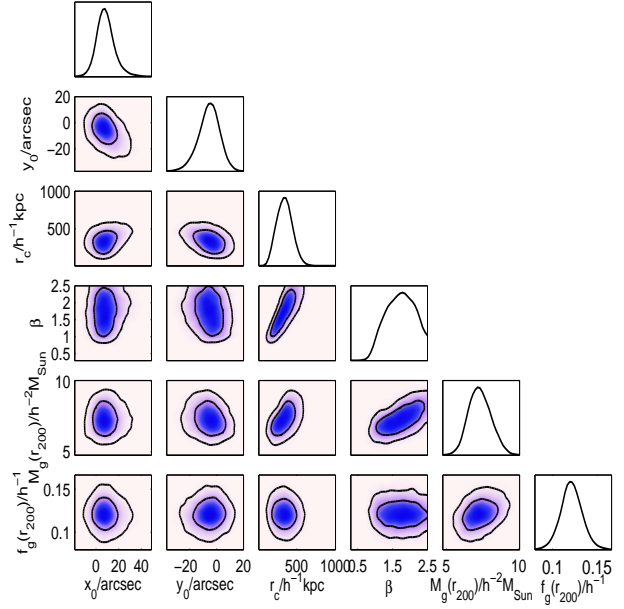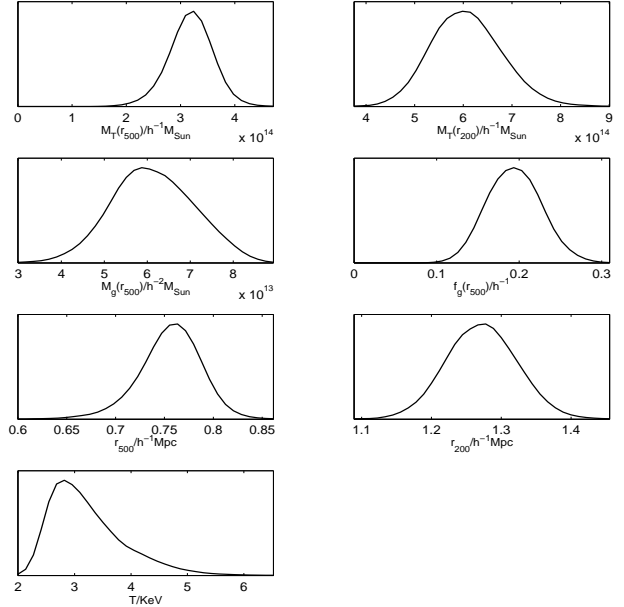

Figure 6. One-dimensional posterior probability distributions for selected derived parameters of Abell 2146—M1. We note that the axes for the plots of the 1-D and 2-D marginalized posterior distributions of both the sampling and derived parameters are tailored to suit the results of each model and will therefore be different in each case

.

the bias on r_X to be propagated to the remaining derived parameters for these values of X.

6.2.2   Cluster model 2

The 2-D and 1-D marginalized posterior probability distributions for the parameters of M2 are depicted in Figs 7 and 8.

M2 introduces a new sampling parameter, $f_g(r_{200})$. Sampling from this parameter allows more prior information to be included

Figure 8. One-dimensional marginalized posterior distributions for the derived parameters of Abell 2146—M2.

in the analysis, which has the effect of constraining the parameter distributions better than in M1. It has a great advantage over M1, namely, the only parameter obtained by assuming hydrostatic equilibrium is the temperature, which is not used explicitly in the calculation of the other derived parameters at r_{200}.

Fig. 9 shows the two-dimensional marginalized posterior distribution for the flux density of source A, S_A, and $M_g(r_{200})$–we choose to plot S_A since source A is the brightest source close to the pointing centre. One can see from Fig. 9 that S_A and $M_g(r_{200})$ do not appear to be significantly correlated. This is confirmed by the sample correlation, which was found to be 0.12. We note that the sample correlation remains unaffected by shifts of origin or changes of scale in S_A and $M_g(r_{200})$. The flux density of source A is given
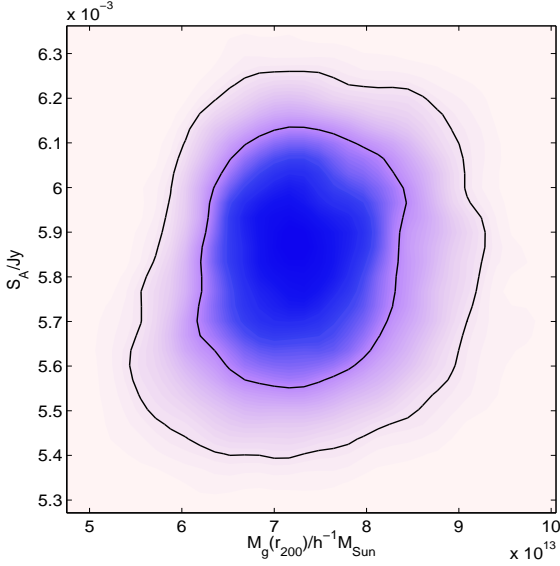
Figure 9. Two-dimensional marginalized posterior distribution for the flux of source A shown in Fig. 3, S_A, and the cluster gas mass within r_{200}, $M_g(r_{200})$.

a Gaussian prior and yet the LA-measured and McAdam-derived flux-density estimates for this source are very close.

6.2.3   Cluster model 3

The 1-D and 2-D marginalized posterior probability distributions for the parameters of M3 are presented in Figs 10 and 11.

The only difference between M2 and M3 is in how the average cluster gas temperature at r_{200}, T, is calculated. To obtain an estimate for T, M2 assumes the cluster is in hydrostatic equilibrium while M3 uses the M-T relation in equation (20), which assumes the cluster is virialized and contains no unseen energy density.

7   DISCUSSION

7.1   Comparison with X-ray maps

Two new Chandra observations of Abell 2146 were taken in April 2009 (Russell et al. 2010). Fig. 13 shows the exposure-corrected X-ray image taken in the $0.3 - 5.0$ keV energy band smoothed with a 2D Gaussian of $\sigma = 1.5$ arcseconds superimposed with the AMI SZ effect from Fig. 3. The AMI uv-coverage is well-filled and goes down to $\approx 180\lambda$ which corresponds to a maximum angular scale of ≈ 10 arcminutes or a cluster radius of ≈ 1.1 Mpc. Thus, in practice, the SZ signal traces a more extended region of the gas than the X-ray data. Any small features in the cluster environment are not resolved by the SA maps which consequently appear much more uniform than the X-ray maps. Nevertheless, given the synthesized beams in Figs. 3 and 4 the SZ effects in these two figures appear to show signs of some real extended emission. To verify that we have resolved the SZ decrement we bin the data from the CLEANed, radio source subtracted, non-tapered map of Abell 2146, Fig. 2, in bins of 100λ and plot it against baseline, see Fig. 12. The signal steadily becomes more negative from scales of 800λ to 200λ; it is on these larger scales that we find the most negative binned value for the SZ decrement, demonstrating the sensitivity of the SA to large angular
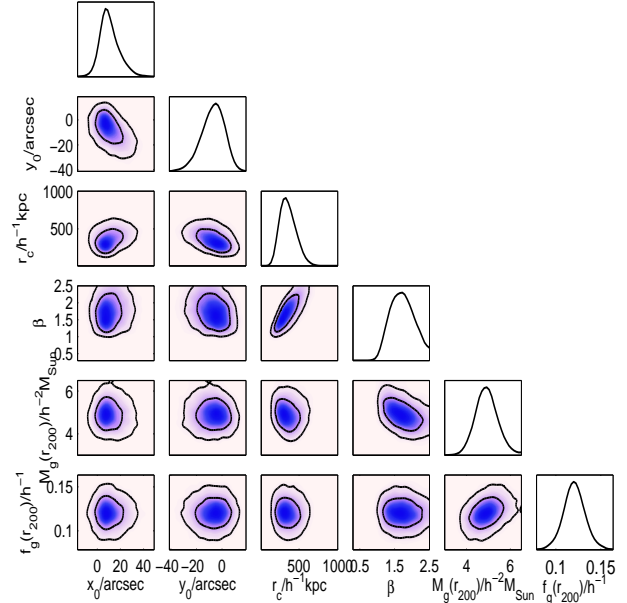

Figure 10. Two-dimensional marginalized posterior distributions for the sampling parameters of Abell 2146—M3.
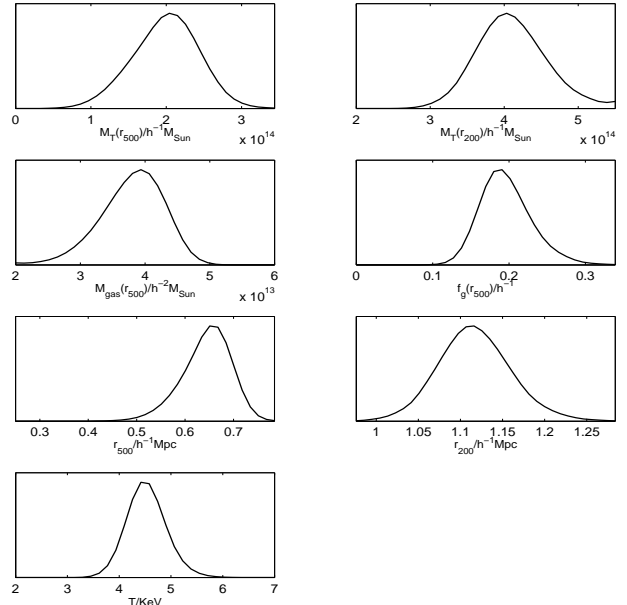
Figure 11. One-dimensional marginalized posterior distributions for the derived parameters of Abell 2146—M3.

scales. To determine the shape of the cluster in greater detail high resolution SZ observations are needed.

During a cluster merger, elongations in the dark matter and gas components are expected. In general, the orientation of this elongation for both components tends to be parallel to the merger axis, though the gas component can also be extended in a direction perpendicular to the merger axis due to adiabatic compressions in the ICM (Roettiger et al. 1997), as shown in simulations of cluster mergers (Poole et al. 2007). We fitted a six-component (position, peak intensity, major and minor axes and position angle) elliptical Gaussian to the SZ decrement in our 0.6 tapered map, Fig. 4, and a zero level using the AIPS task JMFIT. The results for the parameters defining the shape of the fitted ellipse are given in Table 7.
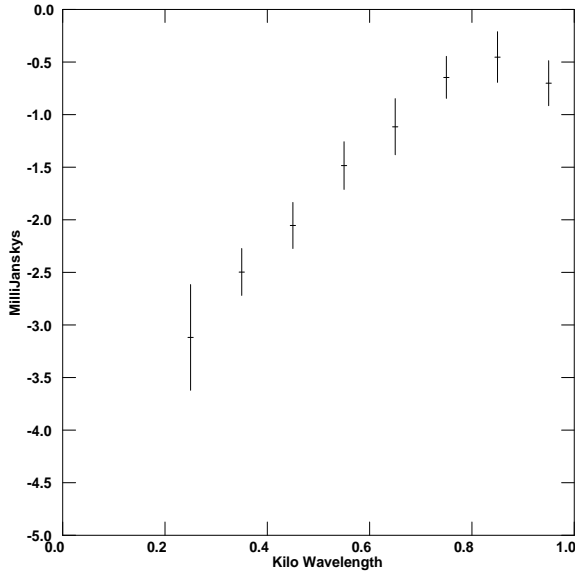
Figure 12. Binned data from the CLEANed, radio source subtracted, non-tapered map of Abell 2146 in bins of 100λ against baseline (in kλ). It should be noted that the FWHM of the aperture illumination function of the AMI SA is $\approx 185\lambda$ such that the visibilities in each bin are not entirely independent. The baseline distance corresponding to the MCADAM derived paremeters r_{200}, r_{500} and r_{1000} were found to be 0.42kλ,0.816kλ, 1.46kλ, respectively.

Table 7. JMFIT results for the parameters of the ellipse fitted to the SZ decrement in the 0.6-tapered SA CLEANed maps. The extension of the minor and major axes are given in arcseconds and the position angle in degrees.

	Nominal	Minimum	Maximum
Major axis	205	171	236
Minor axis	145	109	175
Position angle	46	3	68

The nominal results indicate that the semi-major axis has a position angle of 46°. The orientation of the SZ signal along this axis seems to be $\approx$orthogonal to the elongation of the X-ray signal, see Fig. 13. Shock fronts like the ones observed in Abell 2146 can only be detected during the early stages of the merger, before they have reached the outer regions of the system which suggests that the gas disturbances in the cluster periphery are less intense than those near the dense core.

This is supported by the different signal distributions of the X-ray and SZ effect data. The gas is relatively undisturbed in the cluster periphery while in the inner regions the core passage has displaced the local gas at right angles to the merger axis (Russell et al. 2010).

The total mass can also be estimated from the X-ray $M_{\text{T}}(r_{500})-T$ relation (eg. Vikhlinin et al. (2006)) (note that here we use a different scaling relation than elsewhere since we are concerned with cluster parameters at r_{500}). Excluding the cool core region, the X-ray spectroscopic temperature is 7.5 ± 0.3 keV, which corresponds to a mass $M_{\text{T}}(r_{500}) \approx 7\pm2\times10^{14}M_\odot$ (using $h_{70} = 1.0$). This method will likely overestimate the cluster mass as we expect the temperature to have been temporarily boosted during this major merger by a factor of a few (Ricker & Sarazin (2001), Randall et al. (2002)).
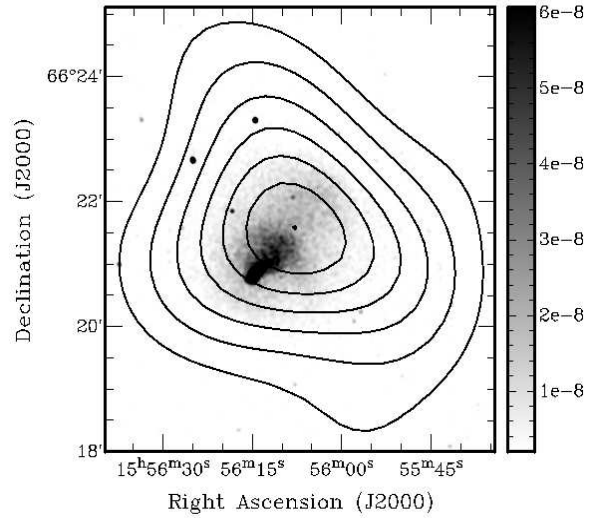

Figure 13. Chandra X-ray image superimposed with AMI SA SZ effect (no taper). The SA map is shown in black contours which go from -1.4 mJy beam^{-1} to 0.001 mJy beam^{-1} in steps of $+0.2$ mJy beam^{-1}. The grey scale shows the exposure-corrected image in the $0.3-5.0$ keV energy band smoothed by a 2D Gaussian $\sigma = 1.5$ arcsec (North is up and East is to the left). The logarithmic scale bar has units of photons cm^{-2}s^{-1}arcsec^{-2}.

A mass estimate for the Bullet cluster from the $M_{\text{T}}(r_{500}) - T$ relation produced a result approximately a factor of 2.4 higher than the weak lensing result for the same region (Markevitch (2006)). If we assume the X-ray mass estimate for Abell 2146 is overestimated by a similar factor, the cluster mass should be closer to $M_{\text{T}}(r_{500}) \approx 3 \times 10^{14}h^{-1}M_\odot$, which is comparable with our SZ effect result. However, simulations show that the transient increase in the X-ray temperature is dependent on the time since the collision, the impact parameter of the merger and the mass ratio of the merging clusters (e.g. Ritchie & Thomas (2002)), which will be different for the Bullet cluster. A weak lensing analysis using new Subaru Suprime-Cam observations will produce a more accurate measure of the mass for comparison with the SZ effect result.

7.2 Comparison with the 4.9-GHz VLA maps

The VLA radio image taken at 4.9-GHz (NRAO/VLA Archive Survey) and the contours representing the LA map are superimposed on the X-ray image in Fig. 15. The presence of a bright source on top of the dense cluster core obscures any possible high-resolution SZ features in the LA map. High-resolution SZ images using the LA would be possible if higher resolution data taken at 16-GHz were available for source subtraction. The longer baselines of the LA proved insufficient to remove the contaminant sources and no SZ effect decrement was seen on the source subtracted LA maps. High-resolution SZ effect measurements are necessary to disentangle the density and temperature distributions properly. These observations in other cluster mergers like the Bullet cluster (Savyasachi et al. 2010) have revealed structure in the gas pressure distribution and are powerful tools for understanding the evolution of galaxy clusters.

Radio halos are faint, large-scale sources that often span the entire cluster and are typically found in cluster mergers. Two hours
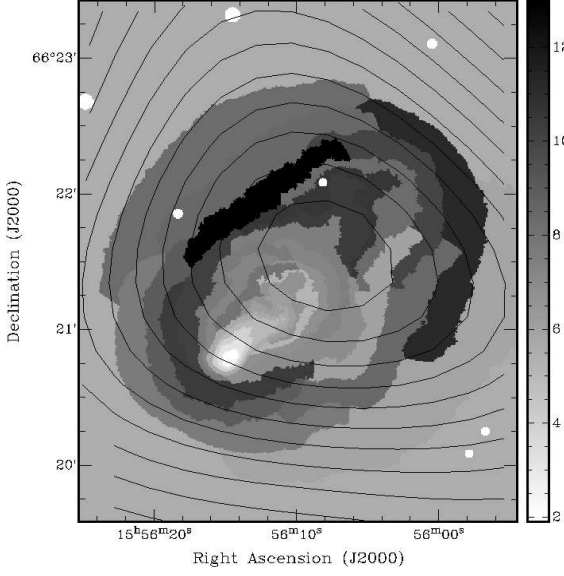
Figure 14. Projected temperature map (keV) (Russell et al. 2010) overlaid on black contours representing the SA SZ effect decrement. The contours go from -1.5 mJy beam^{-1} to 0.1 mJy beam^{-1} in steps of $+0.1$ mJy beam^{-1} and the grey linear scale indicates the temperature variation in keV.

of VLA observations in two configurations, C and D, towards A520 revealed a radio halo with a power of 6.4×10^{24}W Hz^{-1} (Govoni et al. 2001) at 1.4-GHz. The Bullet cluster was also found to have a radio halo with a power of $(4.3 \pm 0.3) \times 10^{25}$ W Hz^{-1} at 1.3-GHz (Liang et al. 2000). No low frequency radio data are currently available for Abell 2146. 4.9-GHz VLA observations of Abell 2146 do not show signs for a radio halo, Fig. 15, though deeper observations, particularly at lower frequencies where radio halo emission tends to be stronger, would be needed to determine whether a radio halo is present in Abell 2146. Since such halos are characterized by a steeply falling spectrum (e.g Hanisch (1980); Govoni et al. (2004)) and no radio halo emission was detected at 4.9-GHz, we do not expect our observations to be contaminated by this diffuse emission.

A520 and 1E0657-56 are the only two clusters that have been found to have both bow shocks and radio halos. They have provided unique information that allows determination of what proportion of the ultrarelativistic electrons producing the radio halo are generated as a result of merger-driven turbulence, as opposed to shock acceleration (Markevitch et al. 2002; Markevitch 2006). Since Abell 2146 is the third cluster merger known to contain substantially supersonic shock fronts, finding a radio halo would significantly improve our current understanding of how they are generated and powered.

7.3 Cluster Parameters

The cluster parameters obtained from M3, our preferred model, are discussed below.

7.3.1 Position

The mean value for the position, RA $15^{\rm h}56^{\rm m}07^{\rm s}$ Dec $+66°21'.33''$, with errors of 6 and 7 arcseconds respectively, coincides with the X-ray centroid position, RA $15^{\rm h}56^{\rm m}07^{\rm s}$ Dec $+66°21'.35''$, as shown
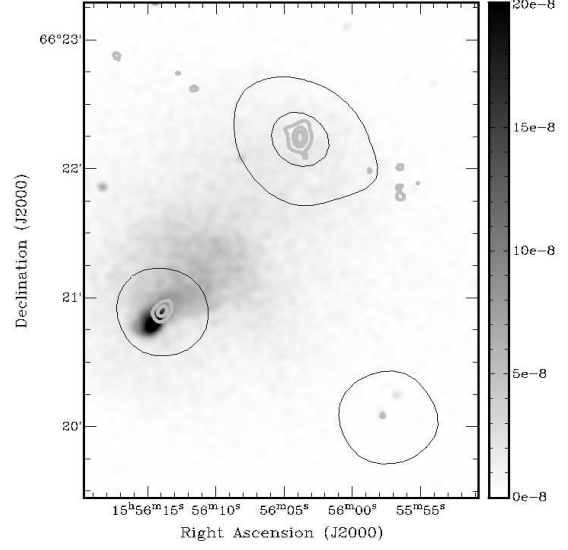
Figure 15. VLA 4.9-GHz map in thick, grey contours overlaid on the AMI LA map, in thin, black contours and the X-ray grey map from Chandra observations. The logarithmic grey scale corresponds to the exposure-corrected X-ray image taken in the $0.3 - 5.0$ keV energy band smoothed with a 2D Gaussian of $\sigma = 1.5$ arcseconds and it is in units of photons cm^{-2}s^{-1}arcsec^{-2}. The VLA and LA contours range from 0.5 mJy beam^{-1} to 9 mJy beam^{-1} in steps of 0.3 mJy beam^{-1}.

in Fig. 13. However, the peak of the X-ray flux is significantly displaced from the peak of the SZ signal, as depicted in Fig. 13. The X-ray spectral luminosity is proportional to $\int n_e^2 T^{-1/2} {\rm d}l$, while the SZ effect is a measure of the integrated line-of-sight pressure and is proportional to $\int n_e T {\rm d}l$. Therefore, the X-ray emission is more sensitive to substructure than the SZ data and peaks at the position of the dense cluster core.

7.3.2 β and r_c

Results from running McADAM on large samples of clusters have forced the prior on β to be relaxed to include higher values (see AMI Consortium: Zwart et al. (2008)). The distributions for β tend to favour higher values than typical X-ray estimates. However, this discrepancy is not surprising since previous studies have revealed incompatibilities in the β fits between X-ray and SZ effect profiles due to their different dependencies on parameters such as temperature and density (Hallman et al. 2007). The results show the degeneracy between r_c and β but also show evidence of strong constraints on this relation. This relation is positively correlated in M1 and M2, where the assumption of hydrostatic equilibrium is made to estimate parameters at r_{200}, and negatively correlated in M3 where this assumption is avoided.

7.3.3 Gas fraction

Sampling from $f_g(r_{200})$ allows further prior information to be introduced into the model which leads to better constrained parameter estimates.

All the models were run through McADAM without data to check the effect of the priors on the results. From this test we discovered that in M1 the seemingly inconspicuous priors on the sampling parameters lead to an effective prior on f_g that peaks around

0.01 and strongly disfavours values of $f_g \approx 0.1$. Since in our current models SZ data alone cannot place strong constraints on f_g, the effective prior biases low the estimates of f_g obtained in M1. On the other hand, when running M3 without data, the effective prior on f_g does not change significantly from the Gaussian prior it was initially given. Given the importance of analysing cluster models without any data to interpret their results, a detailed discussion of these no-data runs and the effects of cluster parameterization are presented in the forthcoming paper, AMI Consortium: Olamaie et al. (2011).

7.3.4 Temperature

The average cluster gas temperature within $r_{200} \approx 900$ kpc for $h_{70} = 1.0$ was found to be 4.5 ± 0.5 keV. The projected emission-weighted temperature map, Fig. 14, shows a range of X-ray temperature measurements in different regions of the cluster. At the position of the most negative value of the SZ decrement, the X-ray temperature is ≈ 8 keV whereas at a radius of ≈ 500 kpc the temperature drops below 5 keV. In Russell et al. (2010), a single-temperature fit to the cluster spectrum of Abell 2146 using an absorbed thermal plasma emission model yields a temperature of $6.7^{+0.3}_{-0.2}$ keV. The higher X-ray temperature measurement is not surprising since M3's derived temperature estimate refers to the mean cluster gas temperature within r_{200} and therefore averages over scales where the temperature is lower. Moreover, emission-weighted temperatures will be higher than mass weighted temperature estimates.

7.3.5 Total mass

Analytical and numerical simulations have already established the integrated SZ signal as a robust tool for determining the total cluster mass (see e.g. Bartlett & Silk (1994); Barbosa et al. (1996); Eke, Cole & Frenk (1996); Da Silva et al. (2000); Kravtsov, Vikhlinin & Nagai (2006); Nagai (2006); Motl et al. (2005)). The measured SZ signal is sensitive to large scales away from the cluster core and is therefore able to provide an estimate for the M_T which is independent of the small-scale mechanisms that regulate the state of the cluster gas near the core.

We find that, subject to the assumptions of M3 described in Section 5.2.3, at the virial radius, r_{200}, $M_T = (4.1 \pm 0.5) \times 10^{14} h^{-1} M_\odot$; note that this estimate is free from the assumption of hydrostatic equilibrium.

8   CONCLUSION

The AMI 16-GHz observations of Abell 2146 presented in this paper show the Sunyaev-Zel'dovich effect produced by this cluster with a peak signal-to-noise ratio of 13σ. We detect 15 4-σ_n sources within 0.1 of the primary beam in the SA pointed map using the high resolution LA observations. These sources were subtracted from the SA maps at the LA position using the flux densities obtained from running our Bayesian analysis software, MCADAM, on the cluster model M3. Despite the substantial radio emission from the direction of Abell 2146, no significant contamination from radio sources is visible on the maps.

We compare our SZ observations with X-ray data taken by Chandra and find an offset between the peaks of the two signals. We show that the SA data resolves our SZ decrement and note that the directions of the most pronounced elongations in the SZ and X-ray

signals seem to be at $\approx 90°$ to each other. These results show complex dynamics indicative of a cluster merger and the differences in the gas emission and pressure distributions.

We run MCADAM, on three different cluster models, all of which assume an isothermal, spherical β-model, and extract posterior probability distributions of large-scale cluster parameters of Abell 2146 in the presence of radio point sources, primordial CMB and receiver noise. In M1, a model representative of more traditional cluster parameterizations, the seemingly inconspicuous priors on the sampling parameters lead to an effective prior on the derived parameter $f_g(r_{200})$ which biases low this parameter and leads to further biases in other model parameters.

M2 and M3 exploit the observation that the gas fractions do not appear to vary greatly between clusters and sample directly from $f_g(r_{200})$—introducing further constraints in our parameter space and avoiding the bias problem in M1. The difference between M2 and M3 lies in the derivation of the global cluster gas temperature, T. M2 assumes the cluster is in hydrostatic equilibrium while in M3 T can be deduced from the virial theorem (assuming all of the kinetic energy is in the form of internal gas energy). Given the relative masses of the two merging systems in Abell 2146 and, provided the primary cluster was virialized before the merger, we find that the T derived from the M-T relation in M3 will change by $\approx 10\%$ K during the merger.

The results from M2 and M3 are consistent, despite differences in the mean values of the large-scale cluster parameters. However, we choose to focus on the results obtained in M3 since this model overcomes some of the shortcomings of more traditional models and its global temperature estimate is not significantly affected by the merger event. We find that at r_{200} $M_T = (4.1 \pm 0.5) \times 10^{14} h^{-1} M_\odot$, $\beta = 1.7 \pm 0.3$, $T = 4.5 \pm 0.5$ keV and core radius $r_c = 358 \pm 100 h^{-1}$ kpc. We also find that the probability of SZ + CMB primordial structure + radio sources + receiver noise to CMB + radio sources + receiver noise is $3 \times 10^6 : 1$.

REFERENCES

Baars J. W. M., Genzel R., Pauliny-Toth I. I. K., Witzel A., 1977, A&A, 61, 99
Barbosa D., Bartlett J. G., Blanchard A., Oukbir J., 1996, A&A, 314, 13
Bartlett J. G., Silk J., 1994, ApJ, 423, 12

Birkinshaw M., 1999, Physical Reports, 310, 97

Birkinshaw M., Lancaster K., 2008, Lecture Notes in Physics, 740, 255

Borgani S., & Guzzo L., 2001, Nature, 409, 39

Browne I. W. A., Wilkinson P. N., Patnaik A. R., Wrobel J. M., 1998, MNRAS, 293, 257G

Cavaliere A. & Fusco-Fermiano R., 1978, A & A, 70, 677

Chieze J-P., Alimi J-M. & Teyssier R, 1998, ApJ, 495, 630

Da Silva A. .C., Barbosa D., Liddle A, Thomas P. A., 2000, MN-RAS, 326, 155

AMI Consortium: Franzen T. M. O. et al., 2010, arXiv:1012.3711

Ebeling, H. and Edge, A. C. and Allen, S. W. and Crawford, C. S. and Fabian, A. C. and Huchra & J. P., 2000, MNRAS, 318, 333

Ebeling H. & Wiedenmann G., 1993, Phys. Rev E., 47, 704

Eke V. R., Cole S. & Frenk C. S., 1996, MNRAS, 282, 263

Feretti L., Giovannini G., 2008, A Pan-Chromatic View of Clusters of Galaxies and the Large-Scale structure, edited by M. Plionis, O. Lopez-Cruz and D. Hughes. Lecture Notes in Physics Vol. 740.474, p.143

Feroz F., Hobson M. P., 2008, MNRAS, 384, 449

Feroz F., Hobson M. P., Bridges M., 2009, MNRAS, 398, 4

Feroz F., Hobson M. P., Zwart T. L. et al., 2009, MNRAS, 398, 2049

Govoni F., Feretti L., Giovannini G., Bohringer H., Reiprich T. H., Murgia M., 2001, A & A, 376, 803

Govono F., Markevitch M., Vikhlinin A., VanSpeybroeck L., Feretti L., Giovannini G., 2004, ApJ, 605, 695

Hanisch R. J., 1980, AJ, 85, 1565

Hallman E. J., Burns J. O., Motl P. M. Norman, Michael L., 2007, ApJ, 665, 911

Hallman E. J., Markevitch M., 2004, ApJ, 610, L81

Hogbom J. A., 1974, A & A. Suppl., 15, 417

Hurley-Walker N., 2009, PhD Thesis, Cambridge University

Liang H., Hunstead R. W., Birkinshaw M., Andreani P., 2000, ApJ, 544, 686

Jeltema T. E., Canizares C. R., Bautz M. W. & Buote D. A., 2005, ApJ, 624, 606

Jones M. E. et al., 1993, Nat, 365, 320

Rines K., Geller M. J., Diaferio A., 2010, ApJ, 715, 2 180-184

Knebe A. & Muller V. , 1999, A & A, 341, 1

Kravtsov A. V., Vikhlinin A., Nagai D., 2006, ApJ, 650, 128

Larson D., Dunkley J., Hinshaw G., Komatsu E. et al., 2010, arXiv:1001.4635

Loken C., Norman M. L., Nelson E., Burns J., Bryan, G. L., Motl P., 2002, ApJ, 579, 571

AMI Consortium: Olamaie M., Rodríguez-Gonzálvez C. et al., 2010, arXiv:1012.4996

Markevitch M. et al., 2000, ApJ, 541, 542

Markevitch M., Gonzalez A. H., David L., Vikhlinin A., Murray S., Forman W., Jones C. & Tucker W., 2002, ApJ, 567, L27

Markevitch M., Vikhlinin A., 2007, Phys. Rep., 443, 1

Markevitch M., in ESA Special Publication, 604, A. Wilson, ed, The X-ray Universe, 2005, 723

Marshall P. J., Hobson M. P. & Slozar A., 2003, MNRAS, 346, 489

Mason B. S., Myers S. T., 2000, ApJ, 540, 614

Maughan B. J., Jones L. R., Forman W. & Van Speybroeck L., 2008, ApJS, 174, 117

Motl P. M., Hallman E. J., Burns J. O, Norman M. L., 2005, ApJ, 623, 63

Nagai D., 2006, ApJ, 650, 538

Nagai D., Vikhlin A & Kravtsov A., 2007, ApJ, 655, 98

Patnaik A. R., Browne I. W. A., Wilkinson P. N., Wrobel J. M., 1992, MNRAS, 254, 655

Gregory B., Poole V., Mark A. et al., 2007, MNRAS, Volume 380, 2,437-454.

Randall S. W., Sarazin C. L. & Ricker P. M., 2002, ApJ, 577, 579

Rasia E., Ettori S., Moscardini L, et al., 2006, MNRAS, 369, 2013

Ricker P. M. & Sarazin C. L., 2001, ApJ, 561, 621

Ritchie B. & Thomas P. A., 2002, MNRAS, 329, 675

Roettiger K., Loken C., & Burns J. O., 1997, ApJSS, 109, 307

Russell, H. R. and Sanders, J. S. and Fabian, A. C. and Baum, S. A. and Donahue, M. and Edge, A. C. and McNamara, B. R. and O'Dea, C. P., 2010, MNRAS

Sarazin C., 1988, X-ray Emission from Clusters of Glaxies, Cambridge University Press

Savyaschi M. S., Subrahmanyan R., Wieringa M, et al., 2010, arXiv:1005.1394

AMI Consortium: Scaife A. M. M., Green D., Pooley G. et al., 2009, MNRAS, 403, 46

Schuecker P., Bohringer H., Voges W., 2004, A & A, 420, 61

Skilling J., Fischer R., Preuss R et al., 2004, AIP Conf. Ser., Bayesian Inference and Maximum Entropy Methods in Science and Engineering. Am. Inst. Phys., New York, 735, 395

Sunyaev R. A., & Zel'dovich Y. B., 1970, Comments on Astrophysics and Space, 2, 66

Takizawa M., 1998, ApJ, 509, 579

Takizawa M., Nagino R. & Matsushita K., 2010, PASJ

Vikhlinin A., Markevitch M., Murray S. S., Jones C., Forman W., Van Speybroeck L., 2005, ApJ, 628, 655

Vikhlinin A., Kravtsov A., Forman W., Jones C., Markevitch M., Murray S. S., Van Speybroeck L., 2006, ApJ, 640, 691

Watson R. A., Carreira P., Cleary K. et al., 2003, MNRAS, 341, 1057

Wilkinson P. N., Browne I. W. A., Patnaik A. R., Wrobel J. M., Sorathia B., 1998, MNRAS, 300, 790

AMI Consortium: Zwart J. T. L., Barker R. W., Biddulph P. et al., 2008, MNRAS, 391, 1545